RESEARCH ARTICLE

ADVANCED ENGINEERING MATERIALS

www.aem-journal.com

Triaxial Residual Stress in Laser Powder Bed Fused 316L: Effects of Interlayer Time and Scanning Velocity

Maximilian Sprengel, Gunther Mohr, Simon J. Altenburg, Alexander Evans,* Itziar Serrano-Munoz, Arne Kromm, Thilo Pirling, Giovanni Bruno, and Thomas Kannengiesser*

The control of residual stress (RS) remains a challenge in the manufacturing of metallic parts using the laser powder bed fusion process (LPBF). This layer-by-layer manufacturing approach gives rise to complex triaxial RS distributions, which require extensive characterization effort for a broader acceptance of LPBF in industry. This study focuses on the distribution of bulk triaxial RS and surface RS in LPBF austenitic steel 316L. The RS are determined by X-ray and neutron diffraction to characterize the RS distribution. Variations in the LPBF parameters interlayer time (ILT) and scanning velocity and their influence on the temperature distribution and resulting RS is investigated using thermographic data from in situ process monitoring. The RS in the LPBF 316L is tensile at the surface and compressive in the bulk. The RS is directly related to the thermal history of the part as shown by the in situ thermography data. Shorter ILT leads to higher temperatures of the part during the manufacturing, which decrease the RS and RS formation mechanisms. Interestingly, the surface RS does not agree with this observation. This study highlights the benefit of using multiple RS determination methods and in situ thermography monitoring to characterize the RS in LPBF processed parts.

1. Introduction

The austenitic stainless-steel alloy 316L is a material of choice when it comes to applications needing high corrosion and oxidation resistance. The range of design flexibility for this material can be further expanded by the use of additive manufacturing (AM) processes such as laser-powder-bed-fusion (LPBF).[1] The unique microstructure features obtained via the layer-by-layer manufacturing manner (i.e., columnar grains, subgrain solidification cellular structures) considerably enhance the yield strength while maintaining a favorable ductility.[2] The quality of a part manufactured by LPBF is however not yet satisfactory, as multiple studies report the formation of pores (which can be deleterious especially if close to the surface), lack of fusion defects (since their stress intensity factor is very high), and high magnitude residual stress (RS), since it offsets nearly all mechanical properties.[3–5] RS is generated because of the nonequilibrium solidification, which leads to inhomogeneous temperature distribution and shrinkage. Since the part is subject to subsequent heating and cooling cycles throughout the building process, the internal stress evolves in such a manner that the final RS distribution is complex. While there are several works showing how to model the RS with reasonably good predictions, the simulation of the LPBF process remains challenging; therefore, experimental data are of great benefit.

There are many influencing factors on the RS among the LPBF process parameters.[6] Many studies report the correlation between scanning strategies and highlight the importance of the scanning vector length on the magnitudes of the RS.[7–11] The scanning strategy and geometry also govern the distribution of the RS, as shown in.[12] Indeed, the scanning strategy and the volumetric energy density (E_v) play a major role on the local heat input. E_v considers the scanning velocity (v), laser power (P), hatch distance (h), and powder layer thickness (t) and is calculated from

$$E_v = \frac{P}{vht} \tag{1}$$

E_v influences the final material properties, e.g., microstructure,[13] mechanical properties,[14] and RS.[15–17] However, it

M. Sprengel, G. Mohr, S. J. Altenburg, A. Evans, I. Serrano-Munoz, A. Kromm, G. Bruno, T. Kannengiesser
Weld Mechanics and Micro Non-Destructive Testing
Bundesanstalt für Materialforschung und -Prüfung (BAM)
Unter den Eichen 87, 12205 Berlin, Germany
E-mail: Maximilian.Sprengel@bam.de; Alexander.Evans@bam.de

T. Pirling
Diffraction
Institut Max von Laue – Paul Langevin (ILL)
71, avenue des Martyrs – CS 20156, Grenoble cedex 9 38042, France

G. Bruno
Institute of Physics and Astronomy
University of Potsdam
Karl-Liebknecht-Straße 24/25, 14476 Potsdam, Germany

T. Kannengiesser
Institute of Materials and Joining Technology (IWF)
Otto von Guericke University of Magdeburg
Universitätsplatz 2, 39106 Magdeburg, Germany

The ORCID identification number(s) for the author(s) of this article can be found under https://doi.org/10.1002/adem.202101330.

DOI: 10.1002/adem.202101330

has now been assessed that E_v does not encompass important process parameters and should not be used as the only metric to assess the future integrity of the part (see[18,19]). Much work has still to be made to explore the enormous process parameter space. As an example, the effect of the interlayer time (ILT) on the RS, indicating the time for powder recoating and laser exposure of a layer,[20] is poorly studied to date. This influencing factor, however, not only gives a measure of the heat dissipation but also gives an indication on how the scaling of the manufacturing process will affect the properties of the final parts. It is as such key to advance the understanding of the LPBF process.

Findings reported in[20–22] show how the ILT, in combination with other parameters, influences the resulting microstructure and the related mechanical properties in Ti-6Al-4V and 316L processed by LPBF. An increase in ILT favors a finer $(\alpha + \beta)$ lamellar structure of Ti-6Al-4V[21,23] and improved ductility.[23] Short ILTs reduce the hardness and enhance the depth of the melt pool with increasing build height in LPBF 316L.[20] The influence of the ILT on the RS, the microstructure, and the mechanical properties of directed-energy deposition (DED) processed alloys, as reported in,[24–28] showed the important role this factor can play in the quality of parts. Even if the thermal history is very different (cooling rates differ by several orders of magnitude) in LPBF compared to DED,[29] it is expected that the ILT can also play an eminent role in the formation of RS in LPBF processed alloys.

A thermography set-up as used in[20,30] can ultimately relate the thermal history to the RS as shown in.[7] Moreover, the RS can be determined using destructive testing (DT), i.e., contour or slitting method, or nondestructive techniques (NDT) such as X-ray diffraction (XRD) and neutron diffraction (ND).[31] In some studies, a combination of the two classes of experimental methods is used and supported by simulations.[32,33] A critical limitation for diffraction techniques to accurately determine RS is the use of an appropriate stress-free-reference d_0.[34] This challenge is harder when using ND, since no simplifying assumptions can be used if one wants to determine a fully triaxial RS. Many studies have successfully shown the suitability of ND to determine the RS in additively manufactured materials.[10,33,35–37]

Nevertheless, the number of studies reporting the distribution of triaxial bulk RS in LPBF 316L parts remains scarce and the influence of the ILT on the RS remains unknown to the author's knowledge. Next to the characterization of the surface and triaxial bulk RS, the influence of variations in the ILT and the E_v (change in the scanning velocity) is also investigated. The macroscopic RS is thereby nondestructively determined by means of XRD and ND. The RS findings are correlated to the thermal process signature monitored by the in situ thermography. The corresponding microstructure characterization is thoroughly reported in.[22]

2. Experimental Section

2.1. Material and LPBF Processing

The objects of investigation of this study were three specimens manufactured by LPBF in two different build jobs. The specimens were built using gas atomized (nitrogen) 316L powder of spherical morphology on a LPBF machine of type SLM280 HL (SLM Solutions Group AG, Lübeck, Germany). The chemical composition of the powder is shown in **Table 1** as analyzed by the supplier (SLM Solutions Group AG). All specimens were manufactured on a stainless steel substrate plate with a preheating temperature of 100 °C. Detailed information about the L-PBF system and the powder properties can be taken from[20] as the same configurations were used in this study.

Table 1. Chemical composition of the 316L powder.

Element	Fe	Cr	Ni	Mo	Mn	Si	C	Mn	P	S	N
wt%	balance	17.7	12.6	2.35	0.92	0.60	0.017	0.92	0.012	0.004	0.1

The build up of rectangular blanks sized 13 mm × 20 mm × 114.5 mm was carried out by using a meander stripe scanning strategy with a 90° rotation between each layer (see **Figure 1**a) without any contour scans. The layer thickness was 50 µm, and the hatch spacing was 120 µm. The single scanning vectors were not interrupted within the cross sections of the part. The individual process conditions (different ILT and scanning velocity) for the three specimens (labeled A, B, and C) are listed in **Table 2**. In the following, the influence of the scanning velocity will be expressed as a change in the E_v. The positions of the specimens A and B were identical. The specimen C was located slightly closer to the center of the build plate. The specimens were heat treated for 4 h at 450 °C and slowly cooled to room temperature before removal from the build plate. This heat treatment is suggested by ASM International for conventionally processed 316L to reduce peak RS.[38] This step was performed to avoid the distortion of the specimens upon removal from the baseplate.

The specimens were then extracted to final dimensions using wire electric discharge machining (WEDM) (Figure 1b). The ND measurements were performed along the building direction (BD, see Figure 1c) at a minimum of 13 locations and in the cross-section 1-1′. Slices (2-2′) of 3 mm thickness were cut from the top and the bottom of the specimens to subsequently extract the stress-free reference d_0 cubes.

2.2. Surface Roughness Measurements

Surface roughness measurements were carried out in alignment with the ISO 11 562[39] standard to permit the comparison of the surface RS between the different specimens with similar surface roughness. The roughness was measured with the contact profilometer Hommel T8000 using the TKL300 probe and assessed with the Turbo Wave V7.59 software (Jenoptik Industrial Metrology GmbH, Villingen-Schwenningen, Germany). The measurements were performed along four lines of 10 mm length with a spacing of 133 µm as shown in **Figure 2**. The roughness measurements were carried out on each lateral surface of the specimen at mid height, corresponding to the measurement location of the RS in plane 1-1′ (Figure 1b).

2.3. Thermography

The thermographic camera was of the type ImageIR8300 (InfraTec GmbH, Dresden, Germany); its sensitivity spans the mid-infrared spectral region (MWIR, 2–5.5 µm). The camera

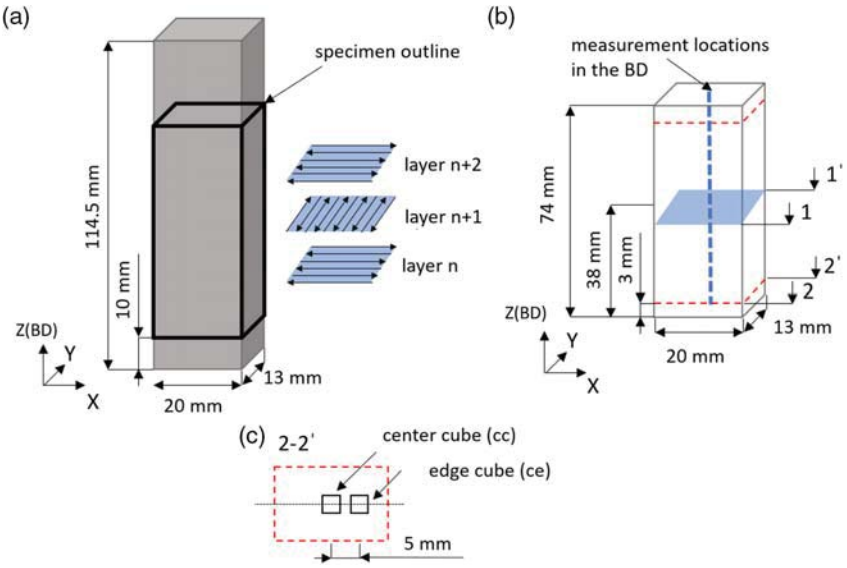

Figure 1. a) As-built dimensions before WEDM extraction of the specimens and meander stripe scanning strategy, b) specimen geometry and dimensions, measurement plane 1-1', measurement line along with the BD, and the location of the 3 mm slices for the extraction of the c) stress-free center (cc) and edge (ce) cubes in the plane 2-2'.

Table 2. LPBF process parameters and description for each specimen.

Specimen ID	Build job	ILT [s]	E_v [J mm^{-3}]	Scanning velocity [mm s^{-1}]	Laser Power [W]
A	1	18 (short)	65 (standard)	700	275
B	2	116 (long)	65 (standard)	700	275
C	2	116 (long)	49 (reduced)	933	275

Table 3. Calibration parameters for postprocessing of the infrared signal.

Specimen	Black body calibration range [K]	Integration time [µs]	Surface emissivity	Build chamber temperature [°C]	Converted calibration range [K]
A	573–873	46	0.23	37.0	721–1221
B and C	473–673	186	0.23	41.7	575–877

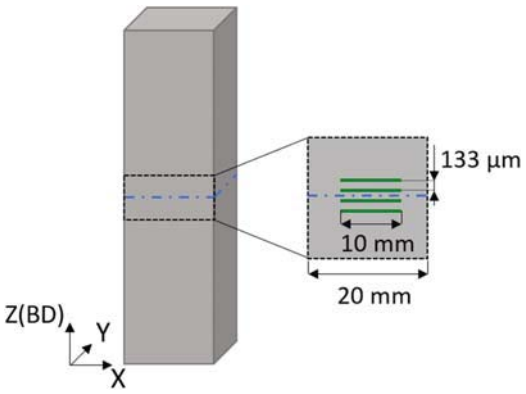

Figure 2. Location of the four surface roughness measurement lines in the *Z-X* and *Z-Y* planes.

was positioned above the ceiling of the LPBF machine to observe the build process via a sapphire window. Two gold plated mirrors in the optical path were used to achieve a perpendicular view on the relevant part of the build plate. The objective had a focal length of 25 mm. A spatial resolution of 420 µm/pixel was reached on the build platform surface. An acquisition frame rate of 600 Hz was set for a subwindow size of 160 × 200 pixels. The set-up of the camera is detailed in.[20]

The calibration parameters shown in **Table 3** were used to convert the readings of the camera during the building process into temperature. To this end, the spectral characteristics of the camera detector and all optical elements were considered. Further details on the postprocessing of the infrared signal are given in.[40]

To gain insight into the variation of the local cooling behavior within a specimen, a local quantity that allows the comparison between the different specimens despite the different temperature history is needed. Here, we calculate the local cooling rate of the specimens at the time t the temperature drops below a value of 80% of the maximum acquired temperature reached in the specimen center. To this end, several data treatment steps were performed. The repeated laser passage at a specific position of the sample leads to rapid heating – cooling cycles (typical repetition rate in the ms range); these are superimposed to the slower heating – cooling cycle (with duration in the 100 ms range) induced by the laser moving to a neighbor region, see the profile of the acquired temperature T_{raw} in **Figure 3**.

Since the cooling rates considered responsible for the creation of the internal stress are rather expected on the latter time and temperature scale, the rapid heating cycles were filtered from the raw data by applying two times a running average filter of 50 ms (30 frames) for each layer. The resulting smoothed temperature is called T_s (red line in Figure 3). Next, the data of each image

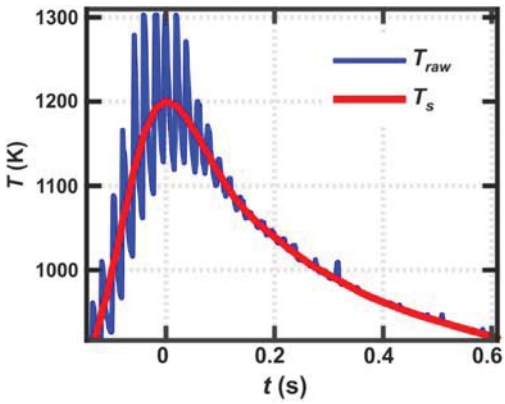

Figure 3. Transient temperature at the center position of a layer production, corresponding to the center of the gauge volume (ND) of the specimen A. Blue line: full time resolution, red line: smoothed temperature.

pixel were shifted along the time axis to place the maximum of T_s at 0 s. This step is needed to average the thermal history at each position over several layers, corresponding to the ND gauge volume height. The average temperature over the gauge volume T_a was calculated for even and odd layers separately to account for possible differences caused by the different lengths of the scan vectors (rotation by 90°, different side lengths of the specimens). Since the temperatures occurring in different samples strongly differ (see Figure 5a), a normalization procedure was performed to reach comparability: First, the maximum smoothed temperature reached at the sample center, $T_{a,max}$, was calculated as reference temperature for each specimen. Next, the cooling rate r when passing the threshold temperature T_{80} was evaluated at all positions (in all specimens). T_{80} is defined as 80% of $T_{a,max}$. The time to reach T_{80} is further defined as t_{80} ($T_{a,max}$ und T_{80} are listed in Table S1, Supporting Information), so that

$$r = \frac{-(T_a(t_{80} - dt) - T_a(t_{80}))}{dt} \tag{2}$$

Note that $T_{a,max}$ and T_{80} differ for each specimen, while t_{80} differs for each position (pixel). Since t_{80} is the last time that T_a reached a value larger than T_{80}, it follows that $T_a(t_{80}) \approx T_{80}$. The time interval dt was set to 100 ms.

2.4. X-Ray Diffraction Measurements

The determination of RS using both the XRD and the ND makes use of Bragg's law to calculate the lattice spacing d of a specific lattice plane, defined by the Miller indices hkl, in knowledge of the wavelength of the radiation λ and of the diffraction angle θ from[41]

$$\lambda = 2d_{hkl}\sin(\theta) \tag{3}$$

The calculation of the RS then differs depending on the diffraction method used. The RS at the surface of the specimens were determined based on the X-ray diffraction $\sin^2\Psi$ method, using a Xstress G3 mobile diffractometer (StressTech Oy, Vaajakoski, Finland). In this method, the normal stress component (out-of-plane) is assumed to be zero. This is directly related to the fact that the radiation used in laboratory XRD set ups only penetrates a few microns in the material. Thus, the fundamental equation of stress calculation using diffraction in the case of plane stress is reduced to

$$\sigma_\Phi = \frac{1}{d_0}\frac{1}{\frac{1}{2}s_2^{311}}\frac{\partial d_\Psi}{\partial \sin^2\Psi} \tag{4}$$

and the RS along the direction Φ can be calculated from the slope of a linear fit to the measured d_Ψ at different Ψ tilts. The standard deviation from the linear fit is a measure of the error. The depth at which the RS were determined was approximately 7 µm. Note that the diffraction elastic constant s_2 depends on the lattice plane used (in our case (311)) for the XRD measurements. For face-centered cubic materials such as the austenitic stainless steel 316L, the use of the 311 reflection has been reported to be a good approximation to determine the macroscopic RS.[42]

2.5. Stress-Free Reference and Neutron Diffraction Measurements

While the d_0 is not of direct importance when determining the *surface* RS (because of the assumption of vanishing normal stress), its influence drastically increases when determining the RS using ND. There are multiple approaches to define a stress-free reference.[43] In the present case, some cubes were extracted at roughly 35 mm from the measurement plane 1-1′, i.e., toward the top and the bottom of the specimen with respect to the BD. Four 3 mm × 3 mm × 3 mm cubes were cut from 3 mm plates from the top and the bottom of the specimens via WEDM (see Figure 1b,c and **Figure 4**). The cubes were therefore assumed to be free of macroscopic stress (it is reasonable to assume that a significant relaxation occurred after cutting) and of similar chemistry and phase distribution as the remaining material. The dimensions of the cubes were chosen to match the gauge volume sized 2 mm × 2 mm × 2 mm. Any remaining stress gradient was therefore assumed to be averaged out. The gauge volume was defined by the collimators P1, P2, and S1 (see Figure 4a) of the Strain Analyser for Large Scale engineering Applications (SALSA) at the Institut Laue Langevin, Grenoble, France.[44] A photo of the sample mount is shown in Figure 4b. The directions of measurements were aligned with the geometrical axes of the specimens and the cubes (see Figure 4a). The results of the cube measurements are shown in Figure 4d: each point represents the average over the three orthogonal measurement directions. Most of the values are within the error bar. For consistency, we are taking for each specimen the same central positioned cube cc from the top slice (shaded in orange) in Figure 4d.

The (normal) strain ε_i for each direction was then calculated at each point in the specimens from

$$\varepsilon_i = \frac{d_i - d_0}{d_0} \tag{5}$$

Subsequently, the triaxial RS is determined assuming isotropic material properties (see[45]) and using Hooke's law

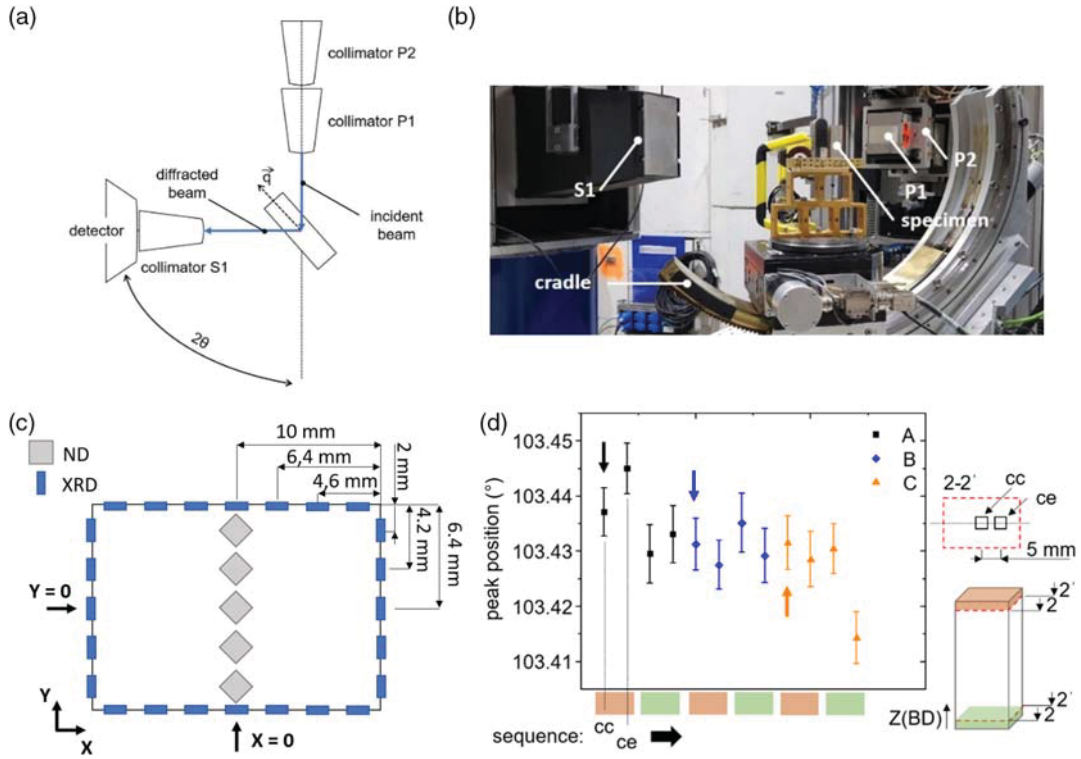

Figure 4. a) ND set-up schematic at SALSA. Primary collimators P1, P2 and secondary collimator S1, b) picture of the SALSA diffractometer, c) ND and XRD measurement positions in the cross-section 1-1′, d) averaged peak positions based on the three measured orthogonal directions of the d_0 corresponding to a short ILT and standard E_v (specimen A), long ILT and standard E_v (specimen B), and long ILT and reduced E_v (specimen C). The d_0 peak positions chosen for the calculation of the RS are indicated by arrows.

$$\sigma_i = \frac{E_{311}}{(1+\nu_{311})(1-2\nu_{311})}[(1-\nu_{311})\varepsilon_i + \nu_{311}(\varepsilon_j+\varepsilon_k)]$$
$$i,j,k \in \mathrm{XX,\ YY,\ ZZ} \quad (6)$$

whereby XX, YY, and ZZ denote the stress components in the *X*-, the *Y*-, and the *Z*-directions (i.e., σ_{XX}, σ_{YY}, and σ_{ZZ} in Figure 4a. The specimens were rotated to align the normal strain direction with the scattering vector *q* (see Figure 4a). The parameters of the measurement set-ups and constants for the calculation of the RS are summarized in **Table 4**. The Young's modulus and Poisson ratio were taken from[46] and were used for the calculation of both the surface RS (XRD) and bulk RS (ND).

The ND and XRD measurement positions in the cross-section 1-1′ (see Figure 1b) at the mid height of the specimens are shown in Figure 4a. The center of mass of the ND measurement positions in the cross sections was 2 mm below the surfaces. The RS in the *Z*-direction were determined at 13 positions at the center of each specimen (see Figure 1b).

Table 4. XRD parameters for surface RS determination.

Measurement mode	$\sin^2\Psi$	Young's modulus E 311 [GPa]	184
Ψ – tilting [°]	−45 to 45 (21 steps)	Poisson's ratio ν_{311}	0.294
Collimator [mm]	2	1/2 s_2 (MPa^{-1})	$7.034\ 10^{-6}$
Reflection/2θ [°]	Fe – 311/152	Radiation	MnKα

3. Results

3.1. In situ Thermography

The averaged smoothed temperature evolutions differ strongly for the specimens A, B, and C. The temperature profiles at the center position of the specimens are depicted in **Figure 5**a. The temperature in the specimen A (short ILT and standard E_v) is higher compared to specimens B (long ILT and standard E_v) and C (short ILT and reduced E_v). The maximum temperature in specimen C and specimen B are approximately at the same level, but the cooling rate is higher in specimen C. The temperature in specimen A remains at a level close to the maximum averaged temperature of specimens B and C. The highest temperatures are reached at the end of the exposure of the surface of the respective specimen (more details given in Figure S1, Supporting Information). The cooling rate maps averaged for even and odd layers of the three specimen A, B, and C are shown in Figure 5b–d. It can be observed that an increase in the normalized cooling rate occurs at the two borders of the specimen that are at the end of the exposure sequence. Additionally, there is a slight increase toward the other two borders and a local maximum at the edge where the scan starts indicated by the white arrows.

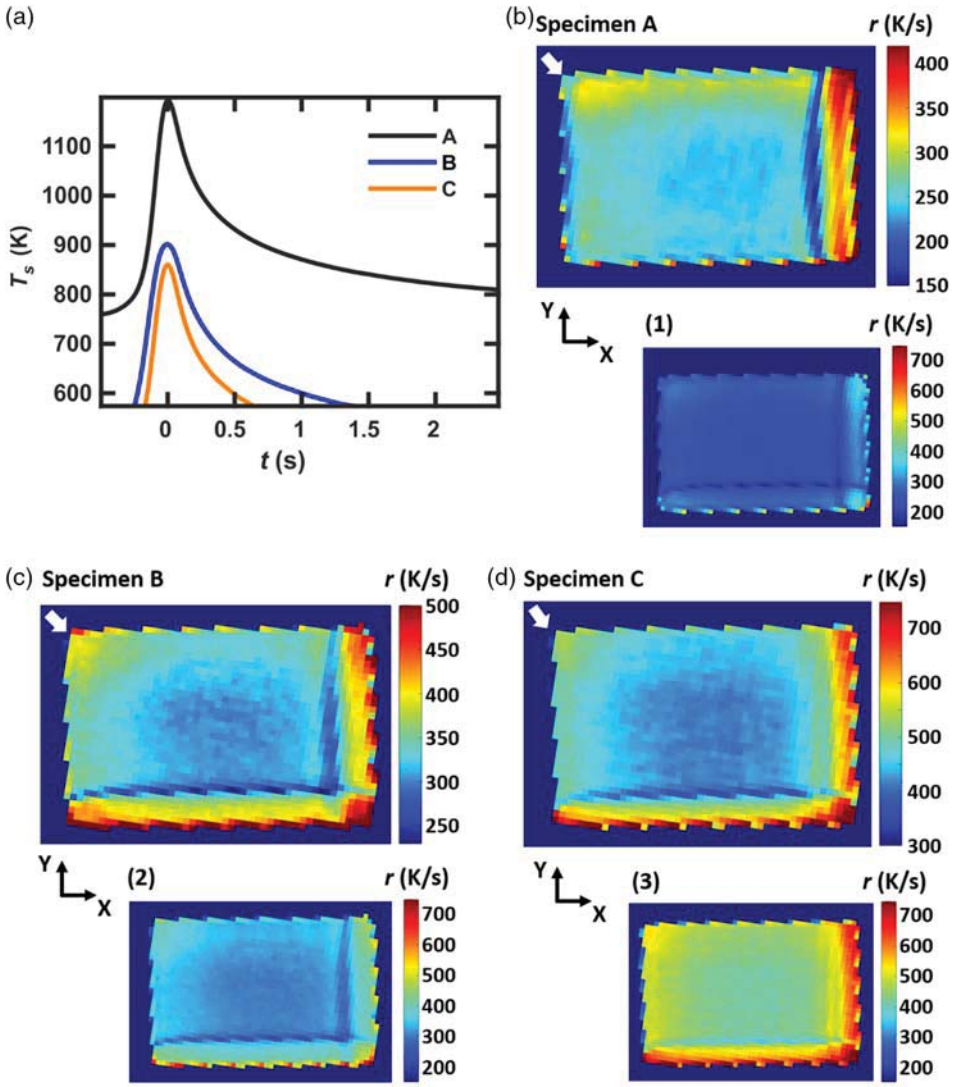

Figure 5. a) Averaged smoothed temperature evolution at the center of the specimens, normalized cooling rate maps, averaged over even and odd layer production in b) the specimen A, c) specimen B and d) the specimen C. The insets 1-3 show the normalized cooling rate maps with identical temperature legends. White arrows indicate local maxima corresponding to the start of even layers.

3.2. Surface Roughness

The surface roughness values *Ra* are shown in **Figure 6**a. The surface (S) ID is given in Figure 6b. *Ra* defines the arithmetic mean values of the measured roughness peaks and valleys. All values lie between approximately 6 and 15 µm. The difference of *Ra* between the four measured surfaces is the largest for the specimen A (short ILT and standard E_v) and the lowest for the specimen C (long ILT and reduced E_v). The *Ra* are nearly constant for the specimen C.

The surface roughness measurements help in the determination of the surface RS: since the radiation used in laboratory XRD only penetrates the material by a few microns, the surface roughness measurements indicate that the RS of specimens A and B can be compared using S2. This strategy allows neglecting the effect of roughness on the determination of the influence of the ILT on the surface RS. Similarly, the surface RS of specimens B and C can be compared using S1, thereby understanding the influence of the scanning velocity on RS. Finally, all specimens can be compared using S4. A summary of the approach is given in **Table 5**.

3.3. Surface Residual Stress

The measurement positions are shown in **Figure 7**a. The influence of the scanning velocity in surface RS can be seen from the results on surface S1 of specimens B and C, shown in Figure 7b. The stress values in specimen B are in general higher than in specimen C for both σ_{ZZ} and σ_{XX}. Almost constant values of RS are observed across the surface for specimen C. The influence of the ILT on the surface RS is analyzed on S2 of specimens A (short ILT) and B (long ILT) in Figure 7c. The σ_{ZZ} and σ_{YY} in

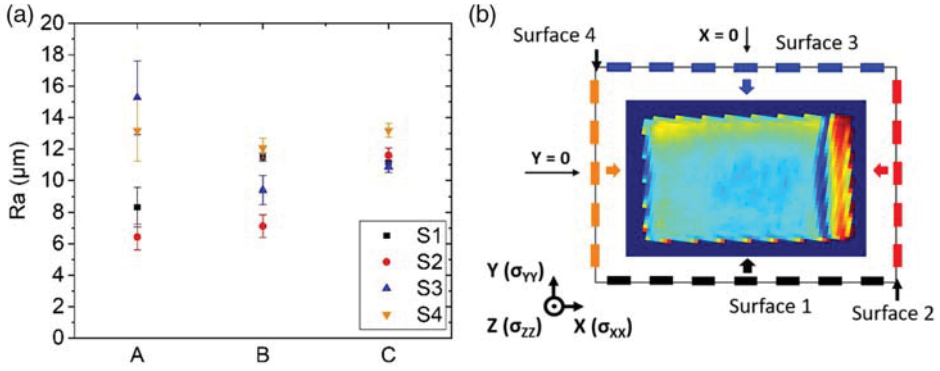

Figure 6. a) Mean roughness values *Ra* of the specimens A, B, and C on each as-built surface of the rectangular geometry, b) ID of the surfaces (S) S1–S4 e.g., surface 1 (S1); XRD measurement positions and the locations of the surfaces correspond to the sketch in Figure 4c. The cooling rate map in b) corresponds to Figure 5b).

Table 5. Surfaces suitable for the comparison of RS, based on the roughness results.

Specimen ID	S1	S2	S3	S4
A	/	X	/	X
B	X	X	/	X
C	X	/	/	X

specimen A are higher than in specimen B. The σ_{ZZ} reaches a maximum of 400 MPa in specimen A. In specimen B, the σ_{ZZ} remains at a broadly constant level around 225 MPa but decrease to 130 MPa at the corner of S3 and S2. The σ_{YY} is lower in magnitude compared to the σ_{ZZ}. In general, the RS values tend to increase toward the center position of the line scan across the surface. In Figure 7d, the σ_{ZZ} and σ_{YY} on S4 are compared among the three specimens. The highest σ_{ZZ} values

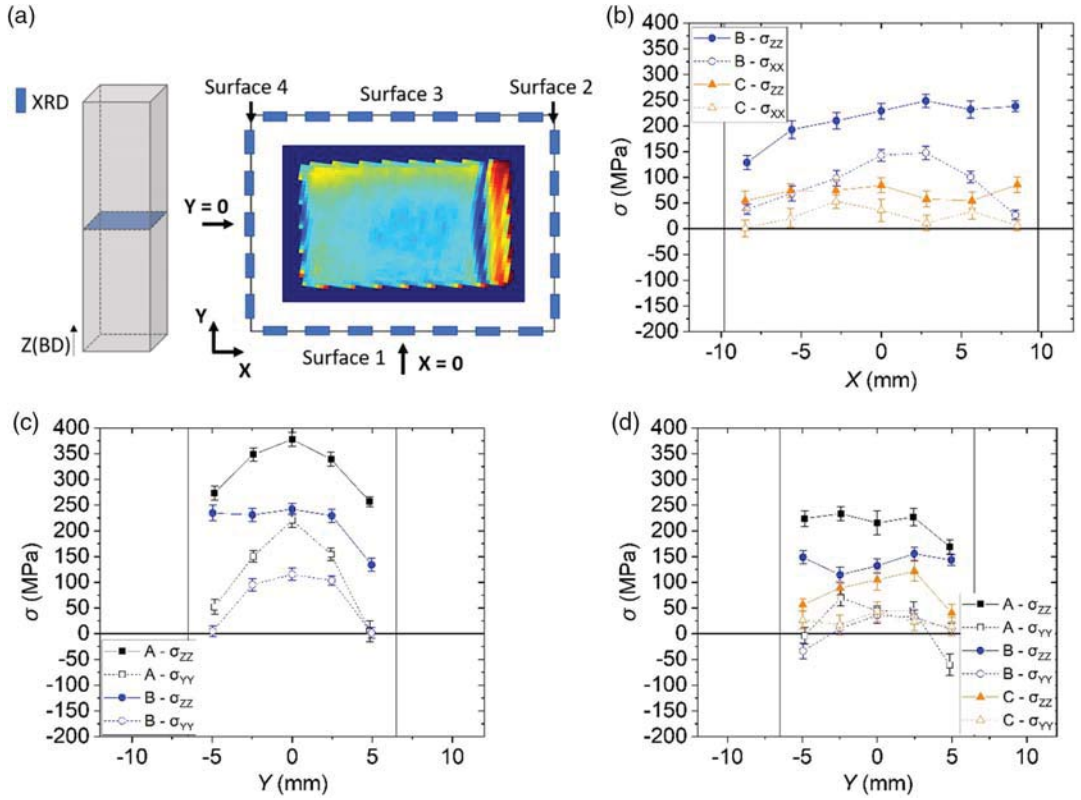

Figure 7. a) XRD measurement points; The cooling rate map in a) corresponds to Figure 5b, b) surface RS of specimens B (long ILT) and C (long ILT and reduced E_v) on S1; c) surface RS of specimens A (short ILT) and B on S2, d) surface RS of all specimens on S4; the error is below 25 MPa. The vertical lines indicate free surfaces.

are found in specimen A, whereas the lowest values are seen in specimen C (short ILT and reduced E_v). The σ_{YY} describe mostly the same trend as observed in σ_{ZZ} but with lower stress values. The σ_{YY} of all specimens are similar on S4, with lower magnitudes.

3.4. Bulk Residual Stress Along the Build Direction

The RS in the *Z*-, the *X*-, and the *Y*-directions at the center of the cross-section along the build height are shown in **Figure 8**. All RS profiles are similar and in each stress direction, the stress values rapidly reach a plateau. For σ_{ZZ}, the values are between −400 and −590 MPa. The highest peak compression value can be found for sample B (long ILT and standard E_v) at −590 MPa. These values are close to the compressive yield strength of LPBF 316L, reported in.[47] The σ_{XX} and σ_{YY} between positions $Z = 20$–50 mm are -150 ± 10 MPa and -70 ± 30 MPa, respectively. A maximum difference of 140 MPa in the *Z*-direction is present between specimen A and specimens B and C. Toward the free surfaces ($Z = 0$ mm, $Z = 68$ mm), the σ_{ZZ} decreases to comply with the stress boundary conditions, and the values of σ_{XX} and σ_{YY} increase to tensile RS.

3.5. Surface and Bulk Through-Thickness Residual Stress in 1-1′

The RS profiles across the thickness (at $X = 0$ mm) of all specimens are shown in **Figure 9**. The σ_{ZZ} displayed in Figure 9b is tensile at the surface. In the subsurface region (2 mm below the surface), the σ_{ZZ} close to S3 is tensile and of higher magnitude compared to the σ_{ZZ} close to S1. Similar observations were reported for LPBF IN718.[48] Around the center, the RS values are compressive. The maximum difference (between specimens A and B) is around 140 MPa (see Figure 9b). The σ_{XX} gradients are U-shaped in the *Y*-direction, reaching a minimum value of about -150 ± 10 MPa. The σ_{YY} in the *Y*-direction increases from compression to tension toward S3 (see Figure 9d). Though the stress boundary conditions are fulfilled in Figure 8, it appears that this is not the case for the σ_{YY} in the *Y*-direction based on a linear extrapolation of the RS to the free surface.

4. Discussion

4.1. Surface and Bulk RS

The analysis of the surface RS shows that the short ILT leads to the highest *surface* RS magnitudes (comparison of the specimens A and B, see Figure 7). Furthermore, increasing the scanning speed leads to lower surface RS (comparison of the specimens B and C, see Figure 7). In the *bulk*, the RS in specimen A (short ILT) are lower compared to the specimens B (long ILT) and C (long ILT and reduced E_v). Moreover, the bulk RS in the specimens B and C are similar. Thus, it appears that the surface and bulk RS evolve somewhat independently. One possibility to explain this behavior could be the use of erroneous d_0. In our study, we observed relatively constant d_0 reference values (see Figure 4d) between two in-plane positions. Moreover, the σ_{ZZ} distribution in Figure 8b at the central location is considered to substantiate the ND measurements, since the stress seems to

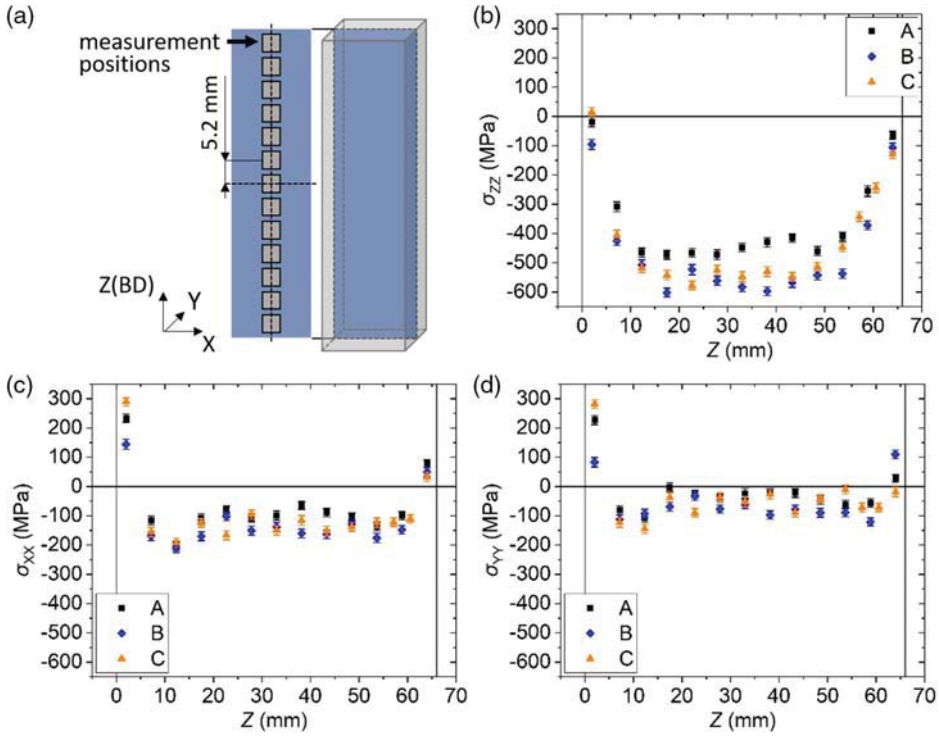

Figure 8. a) ND measurement positions in the Z-direction, b) σ_{ZZ}, c) σ_{XX}, and d) σ_{YY} determined by ND at the center position of the specimens along with the build height. The vertical lines demark the WEDM cut faces ($Z = 0$ mm, $Z = 68$ mm).

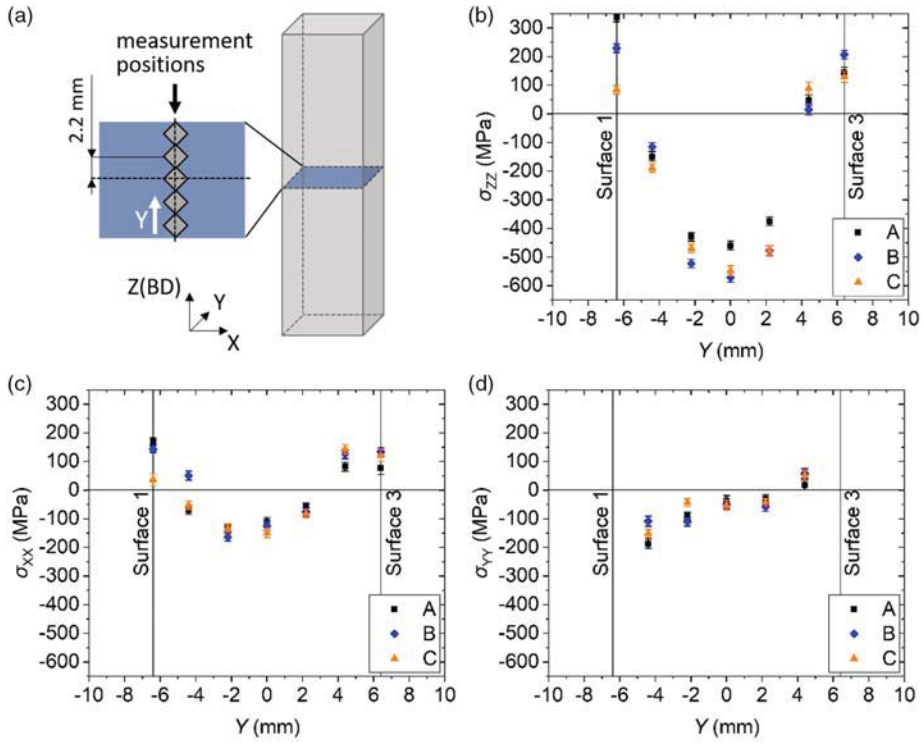

Figure 9. a) Through thickness RS measurement positions, b) σ_{ZZ}, c) $\sigma_{XX,}$ and d) σ_{YY} profiles through the thickness ($X = 0$ mm) determined by ND; the error is below 20 MPa.

satisfy the boundary conditions (zero stress at the free surface). We note that the σ_{YY} should in theory be symmetric with respect to the geometrical axes, but it is not in Figure 9d; σ_{YY} should also be small close to the surface (see Figure 9d). At a first glance, one can consider unlikely that the difference between the ND and XRD trends and the asymmetry of the through-thickness RS profiles could be caused by locally changing d_0 values not captured using the cubes (see Figure 1c). In fact, a study on LPBF IN718 showed that d_0 reference values were similar along a cross-section at half the height of a specimen (20 mm in height and width).[48] However, looking at the thermography maps in Figure 5, there is an asymmetry in the cooling rate along the scan direction. If maintained along the whole build direction, such asymmetry could build up to an asymmetry of d_0. The observed asymmetry could also result from a redistribution and relaxation of the RS following the specimen preparation (because of the removal from the base plate).[37] The redistribution was reported to be limited to the RS close to the cut surface,[37] which is also observed in Figure 8 (see σ_{XX} and σ_{YY}). Finally, the asymmetric RS profiles in Figure 8 (surface RS in specimen B) and Figure 9 (bulk RS in all specimens) could also be a result of the scanning strategy that may lead to nonaxisymmetric distributions of RS (see subsection 4.2), as already shown in.[49] Definitely, further characterization efforts are necessary to elucidate these scenarios.

In any case, to perform an unbiased comparison (i.e., without the influence of d_0) of the bulk RS between the specimens, in the remainder of the paper, RS *ranges* are used. The RS range is defined by the difference between the maximum and minimum bulk RS values.

Investigating solely the surface RS would have resulted in correlating shorter ILT with overall higher RS magnitudes contrary to what we observe for the bulk. In fact, specimen B was manufactured with a longer ILT and the bulk RS are higher compared to specimen A. Moreover, a recent study concluded that the heat treatment at 450 °C for 4 h had only a minor effect on the RS.[50] Therefore, it is considered that the differences in RS magnitudes are directly related to the variations in ILT and E_v.

4.2. Influence of the Interlayer Time

The surface RS seems to evolve in an opposite trend compared to the bulk RS. This has also been observed in the study on the helix scanning strategy in[7] and for the DED of IN625 in.[28] A shorter ILT leads to higher surface RS but lower compressive bulk RS. The influence of the roughness[19] is suppressed in this study by comparing solely surfaces that exhibit similar R_a. Therefore, it is reasonable to state that the different surface RS is genuinely due to the thermal evolution resulting from the scanning strategy. Other parameters such as the build position,[18] gas flow orientation,[19] and inclination of the incident laser beam[18] are assumed to have played a negligible role, as specimens B and C were built close to each other on the build plate. Specimens A and B share the same build position (the build job was different, but it has been shown that different build jobs yield the same RS, if run with the same parameters[18]). Within one layer, the heat accumulates differently depending on the position in the cross-section of the specimen, resulting in varying maximum temperatures, as shown in **Figure 10**a (even layers) and b

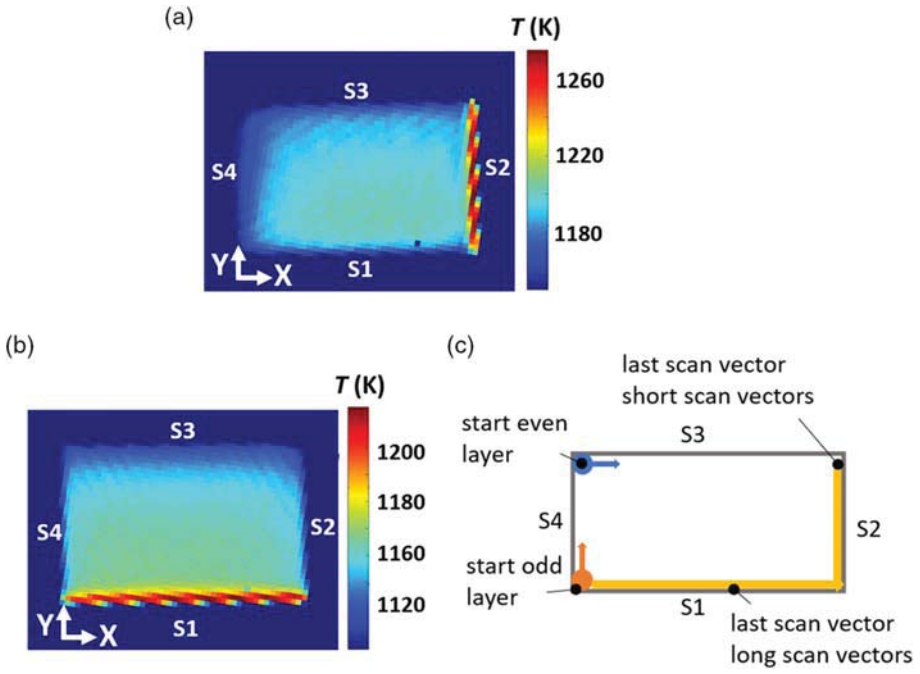

Figure 10. a) Illustration of the scan strategy for even and odd layers. Specimen A: b) maximum averaged temperature for even layers, c) maximum averaged temperatures for odd layers.

(odd layers). Figure 10c illustrates the start and end positions during exposure for even and odd layers. An increased heat accumulation at the end of the exposure of a specimen is reasonable, since here the sample is already heated from the exposure of the previous layer and the heat cannot dissipate well in the surrounding powder bed.[51] The heat accumulation, however, affects the main RS formation mechanisms during LPBF. In LPBF, the combination of the thermal gradient mechanism (TGM) and the constrained shrinkage (CS) or cool down model is often used to explain the formation of RS.[7,52] The TGM explains how RS form when a steep thermal gradient leads to a dissimilar expansion and contraction. This effect ultimately gives rise to inelastic strains within the material and ultimately to RS.[53] Furthermore, the CS is also affected by temperature gradients, due to the temperature dependence of material properties such as Young's modulus and yield strength. A temperature of around 520 °C (as observed in specimen A[22]) was found to reduce the yield strength of LPBF 316L by about 45% as reported in.[54] It can be assumed that the heat accumulation in specimen A slightly reduces the RS, i.e., results in compressive RS of lower magnitude compared to specimens B and C. The difference in σ_{ZZ} in the *Z*-direction between the specimens A and B is shown in **Figure 11**. The heat accumulation and resulting reduction of the yield strength may act as a boundary for the accumulation of internal stress.[55] In an analogy to stress-relief heat treatments, the build-up or relaxation of internal stress is linked to the yield strength. During manufacturing, internal stress is relaxed through plastic deformation once reaching the temperature-dependent yield strength. This consequently lowers the elastic strains in the part, thereby yielding lower RS.

Moreover, since the manufacture of the specimens takes several hours (10–12 h for specimen A), it is further conceivable that the elastic strains are reduced through creep-like relaxation[56,57] (whereby the internal stress plays the role of the applied load). Once room temperature is reached, the reduction of elastic strain in the specimen leads to lower RS. For comparison, it has been shown that a higher powder bed temperature through base plate heating or the preheating of the layer (electron beam melting (EBM)) increases the temperature of the specimen and results in lower RS.[52,58,59] Therefore, the ILT appears to have a similar effect as increasing the powder bed temperature or the preheating of the layer in EBM.

However, specimen A exhibits the highest *surface* RS in an area of accumulated heat (S2). This fact is also observed in specimen B. Higher σ_{ZZ} on S1 compared to S4 are also observed. Since the S1 (Figure 10c) corresponds to a region of accumulated heat (Figure 10b), one could have assumed lower RS compared to S4. The analysis of the cooling rates (see Figure 5b–d) might explain why the surface RS are higher in specimen A. We observe an overall higher heat accumulation at S2 of specimen A (see Figure 10a), which is also characterized by lower cooling rates compared to specimen B (Figure 5b,c). Upon further cooling, the difference in cooling rates between the bulk and the surface could possibly be higher in specimen A. Regions that stay longer at a higher temperature are subsequently constrained in shrinkage by the colder adjacent material; this temperature mismatch results in higher *surface* RS.[60] Further analysis of the cooling of one layer over the full ILT would be required to validate this scenario. Moreover, the thermography set-up used for monitoring the manufacturing of all specimens has a resolution of 420 µm/pixel. Since X-rays penetrate a shallow material layer (≈5–10 µm), a direct comparison between the surface RS and thermography data remains difficult.

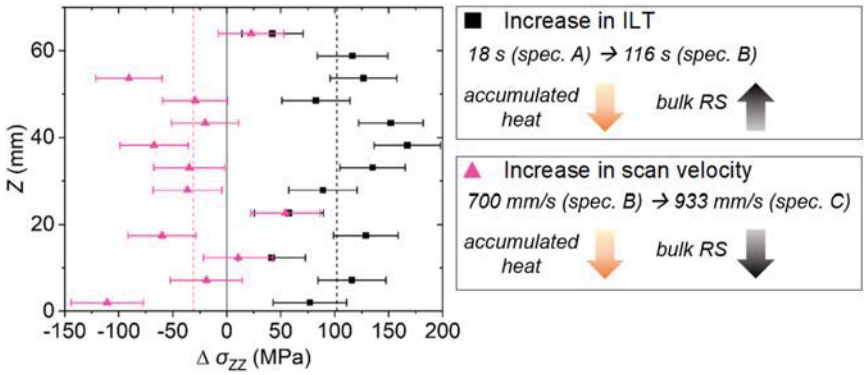

Figure 11. Summary of the influence of ILT and change in scanning velocity on the *bulk* σ_{ZZ}. The difference in σ_{ZZ} along the BD is compared to illustrate an increase in ILT (difference between specimens A and B, black squares) and increase in scanning velocity (difference between specimens B and C, purple triangles).

4.3. Influence of the Scanning Velocity

It is generally accepted that a faster cooling of the material leads to a faster solidification, steeper thermal profiles, and thus higher RS magnitudes.[9] Specimens B and C share the same ILT, but the lower E_v (larger laser velocity) in specimen C results in a lower heat accumulation and higher cooling rates (see Figure 5). As a result, the surface RS and bulk RS range would be expected to be larger in specimen C compared to specimen B (all measurement points considered). However, the surface RS are lower in specimen C (up to 100 MPa in σ_{ZZ}), but the bulk RS difference between these two samples is minor. In fact, the comparison of the RS distribution along the build height between the two specimens (see Figure 11) shows slightly lower RS for sample C (in average 30 MPa). Therefore, increasing the scanning velocity by $\approx$200 mm s^{-1} does not seem to lead to substantial variations in the bulk RS. The comparison of the specimens B and C with respect to specimen A (short ILT) confirms the trend that a lower heat accumulation during manufacturing results in larger *bulk* RS ranges. It furthermore highlights the difference in the information derived from the surface and bulk RS.

5. Conclusions

The RS were determined by means of X-ray and neutron diffraction[61] in specimens manufactured using different ILT and E_v, while keeping specimen geometries and scanning strategies identical. The RS results were discussed on the base of in situ thermal monitoring data obtained during manufacturing. The following observations were made: 1) The increase of the ILT leads to a 10% increase in the bulk RS range. The RS is compressive in the bulk (≈-560 MPa) and tensile ($\approx$300 MPa) at the surface. 2) Reducing the volumetric energy density E_v by increasing the scanning velocity further increases the range of the RS (difference between maximum and minimum value). 3) Based on in situ thermography data, we could deduce that the RS tends to be of highest magnitude in specimens accumulating lower levels of heat. This observation was explained using two mechanisms: a) in analogy to stress-relief heat treatments, specimens exposed at high temperatures for long manufacturing times undergo creep, so that the elastic strains are reduced. Moreover, the higher the bulk temperature, the lower the yield strength at temperature, so that the resulting RS is lower. b) Heat accumulation reduces the sources for the formation of RS, i.e., lower thermal gradients and lower elastic modulus and yield strength. 4) The trend observed for surface RS is in contradiction to that of the bulk RS. The different behavior of the surface RS might be a result of the heterogeneous layer manufacture and subsequently local variations in thermal gradients as shown by the in situ thermography.

This study clearly shows the benefit of correlating in situ monitoring with post-process properties such as RS. The possibility to monitor how the heat accumulates and distributes during the manufacturing enables conclusions to be drawn regarding the RS that would not be otherwise possible.

Supporting Information

Supporting Information is available from the Wiley Online Library or from the author.

Acknowledgements

This work was funded by the BAM Focus Area Materials project AGIL "Microstructure Development in Additively Manufactured Metallic Components: from Powder to Mechanical Failure" and ProMoAM "Process monitoring of Additive Manufacturing". The authors are thankful for the financial support and the fruitful cooperation with all partners. This work is based upon experiment 1-02-276 performed at the SALSA instrument operated by the Institut-Laue-Langevin, Grenoble, France.

Open access funding enabled and organized by Projekt DEAL.

Conflict of Interest

The authors declare no conflict of interest.

Data Availability Statement

The data that support the findings of this study are available from the corresponding author upon reasonable request.

Keywords

in situ thermography, interlayer time, laser powder bed fusions, triaxial residual stresses, X-ray and neutron diffractions

Received: September 29, 2021
Revised: November 17, 2021
Published online:

[1] Y. M. Wang, T. Voisin, J. T. McKeown, J. Ye, N. P. Calta, Z. Li, Z. Zeng, Y. Zhang, W. Chen, T. T. Roehling, R. T. Ott, M. K. Santala, P. J. Depond, M. J. Matthews, A. V. Hamza, T. Zhu, *Nat. Mater.* **2018**, *17*, 63.
[2] D. Kong, C. Dong, S. Wei, X. Ni, L. Zhang, R. Li, L. Wang, C. Man, X. Li, *Addit. Manuf.* **2021**, *38*, 101804.
[3] N. Haghdadi, M. Laleh, M. Moyle, S. Primig, *J. Mater. Sci.* **2020**, *56*, 64.
[4] T. DebRoy, H. L. Wei, J. S. Zuback, T. Mukherjee, J. W. Elmer, J. O. Milewski, A. M. Beese, A. Wilson-Heid, A. De, W. Zhang, *Prog. Mater. Sci.* **2018**, *92*, 112.
[5] J. L. Bartlett, X. Li, *Addit. Manuf.* **2019**, *27*, 131.
[6] Z.-C. Fang, Z.-L. Wu, C.-G. Huang, C.-W. Wu, *Opt. Laser Technol.* **2020**, *129*, 106283.
[7] A. Ulbricht, S. J. Altenburg, M. Sprengel, K. Sommer, G. Mohr, T. Fritsch, T. Mishurova, I. Serrano-Munoz, A. Evans, M. Hofmann, G. Bruno, *Metals* **2020**, *10*, 1234.
[8] D. Wang, S. Wu, Y. Yang, W. Dou, S. Deng, Z. Wang, S. Li, *Materials* **2018**, *11*, 1821.
[9] J.-P. Kruth, J. Deckers, E. Yasa, R. Wauthlé, *Proc. Inst. Mech. Eng., Part B: J. Eng. Manuf.* **2012**, *226*, 980.
[10] A. S. Wu, D. W. Brown, M. Kumar, G. F. Gallegos, W. E. King, *Metall. Mater. Trans. A* **2014**, *45*, 6260.
[11] P. Bian, J. Shi, Y. Liu, Y. Xie, *Opt. Laser Technol.* **2020**, *132*, 106477.
[12] L. A. Parry, I. A. Ashcroft, R. D. Wildman, *Addit. Manuf.* **2019**, *25*, 166.
[13] W. Xu, M. Brandt, S. Sun, J. Elambasseril, Q. Liu, K. Latham, K. Xia, M. Qian, *Acta Mater.* **2015**, *85*, 74.
[14] E. Liverani, S. Toschi, L. Ceschini, A. Fortunato, *J. Mater. Process. Technol.* **2017**, *249*, 255.
[15] I. Serrano-Munoz, T. Mishurova, T. Thiede, M. Sprengel, A. Kromm, N. Nadammal, G. Nolze, R. Saliwan-Neumann, A. Evans, G. Bruno, *Sci. Rep.* **2020**, *10*, 14645.
[16] T. Thiede, S. Cabeza, T. Mishurova, N. Nadammal, A. Kromm, J. Bode, C. Haberland, G. Bruno, *Mater. Perform. Charact.* **2018**, *7*, 717.
[17] K. Artzt, T. Mishurova, P.-P. Bauer, J. Gussone, P. Barriobero-Vila, S. Evsevleev, G. Bruno, G. Requena, J. Haubrich, *Materials* **2020**, *13*, 3348.
[18] T. Mishurova, K. Artzt, J. Haubrich, G. Requena, G. Bruno, *Addit. Manuf.* **2019**, *25*, 325.
[19] T. Mishurova, K. Artzt, J. Haubrich, G. Requena, G. Bruno, *Metals* **2019**, *9*, 261.
[20] G. Mohr, S. J. Altenburg, K. Hilgenberg, *Addit. Manuf.* **2020**, *32*, 101080.
[21] W. Xu, E. W. Lui, A. Pateras, M. Qian, M. Brandt, *Acta Mater.* **2017**, *125*, 390.
[22] G. Mohr, K. Sommer, T. Knobloch, S. J. Altenburg, S. Recknagel, D. Bettge, K. Hilgenberg, *Metals* **2021**, *11*, 1063.
[23] E. W. Lui, W. Xu, A. Pateras, M. Qian, M. Brandt, *JOM* **2017**, *69*, 2679.
[24] J. P. Oliveira, T. G. Santos, R. M. Miranda, *Prog. Mater. Sci.* **2020**, *107*, 100590.
[25] A. Yadollahi, N. Shamsaei, S. M. Thompson, D. W. Seely, *Mater. Sci. Eng. A* **2015**, *644*, 171.
[26] L. Sorkhi, J. J. Hammell, G. A. Crawford, *Metall. Mater. Trans. A* **2020**, *51*, 4390.
[27] B. Torries, S. Shao, N. Shamsei, S. M. Thompson, *Solid Freeform Fabrication Symp.*, University of Austin, Austin, Texas **2016**, pp. 1272–1282.
[28] E. R. Denlinger, J. C. Heigel, P. Michaleris, T. A. Palmer, *J. Mater. Process. Technol.* **2015**, *215*, 123.
[29] H. L. Wei, H. K. D. H. Bhadeshia, S. A. David, T. DebRoy, *Sci. Technol. Weld. Joining* **2019**, *24*, 361.
[30] G. Mohr, N. Scheuschner, K. Hilgenberg, *Procedia CIRP* **2020**, *94*, 155.
[31] P. J. Withers, H. K. D. H. Bhadeshia, *Mater. Sci. Technol.* **2001**, *17*, 355.
[32] J. Mathew, R. J. Moat, S. Paddea, J. A. Francis, M. E. Fitzpatrick, P. J. Bouchard, *Metall. Mater. Trans. A* **2017**, *48*, 6178.
[33] R. J. Moat, A. J. Pinkerton, L. Li, P. J. Withers, M. Preuss, *Mater. Sci. Eng. A* **2011**, *528*, 2288.
[34] T. Mishurova, I. Serrano-Muñoz, T. Fritsch, A. Ulbricht, M. Sprengel, A. Evans, A. Kromm, M. Madia, G. Bruno, in *Structural Integrity of Additive Manufactured Materials & Parts*, ASTM International, West Conshohocken, PA **2020**, pp. 122–138.
[35] F. Bayerlein, F. Bodensteiner, C. Zeller, M. Hofmann, M. F. Zaeh, *Addit. Manuf.* **2018**, *24*, 587.
[36] D. W. Brown, J. D. Bernardin, J. S. Carpenter, B. Clausen, D. Spernjak, J. M. Thompson, *Mater. Sci. Eng. A* **2016**, *678*, 291.
[37] R. J. Williams, F. Vecchiato, J. Kelleher, M. R. Wenman, P. A. Hooper, C. M. Davies, *J. Manuf. Pro.* **2020**, *57*, 641.
[38] J. Douthett, in *ASM Handbook*, ASM International, West Ohio **1991**, pp. 1682–1708.
[39] ISO-11562, International Organization for Standardization, Geneva, **1996**.
[40] G. Mohr, S. Nowakowski, S. J. Altenburg, C. Maierhofer, K. Hilgenberg, *Metals* **2020**, *10*, 1546.
[41] W. H. Bragg, W. L. Bragg, *Proc. R. Soc. A* **1913**, *88*, 428.
[42] M. R. Daymond, M. A. M. Bourke, R. B. Von Dreele, B. Clausen, T. Lorentzen, *J. Appl. Phys.* **1997**, *82*, 1554.
[43] ISO-21432, International Organization for Standardization, Geneva, **2019**.
[44] T. Pirling, G. Bruno, P. J. Withers, *Mater. Sci. Eng. A* **2006**, *437*, 139.
[45] T. Mishurova, G. Bruno, S. Evsevleev, I. Sevostianov, *J. Appl. Phys.* **2020**, *128*, 025103.
[46] P. Rangaswamy, M. L. Griffith, M. B. Prime, T. M. Holden, R. B. Rogge, J. M. Edwards, R. J. Sebring, *Mater. Sci. Eng. A* **2005**, *399*, 72.
[47] W. Chen, T. Voisin, Y. Zhang, J.-B. Florien, C. M. Spadaccini, D. L. McDowell, T. Zhu, Y. M. Wang, *Nat. Commun.* **2019**, *10*, 4338.
[48] I. Serrano-Munoz, A. Evans, T. Mishurova, M. Sprengel, T. Pirling, A. Kromm, G. Bruno, *Adv. Eng. Mater.* **2021**.
[49] J. L. Bartlett, B. P. Croom, J. Burdick, D. Henkel, X. Li, *Addit. Manuf.* **2018**, *22*, 1.
[50] M. Sprengel, A. Ulbricht, A. Evans, A. Kromm, K. Sommer, T. Werner, J. Kelleher, G. Bruno, T. Kannengiesser, *Metall. Mater. Trans. A* **2021**, *52*, 5342.
[51] S. J. Altenburg, N. Scheuschner, C. Maierhofer, G. Mohr, K. Hilgenberg, *Conf. Proc. 15th Quantitative InfraRed Thermography conf.*, Porto, Portugal **2020**.
[52] P. Mercelis, J.-P. Kruth, *Rapid Prototyping J.* **2006**, *12*, 254.
[53] S. P. Edwardson, J. Griffiths, G. Dearden, K. G. Watkins, *Phys. Procedia* **2010**, *5*, 53.
[54] B. Diepold, S. Neumeier, A. Meermeier, H. W. Höppel, T. Sebald, M. Göken, *Adv. Eng. Mater.* **2021**, 2001501.
[55] J. E. Agapakis, K. Masubuchi, *Welding J.* **1984**, *63*, 187.

[56] J. Hoffmann, B. Scholtes, O. Voehringer, E. Macherauch, in *Internation Conference On Residual Stresses* (Eds: E. Macherauch and V. Hauk), Deutsche Gesellschaft für Materialkunde, Garmisch-Partenkirchen, **1986**.
[57] G. Totten, M. Howes, T. Inoue, ASM International Publishers, USA **2002**, pp. 417–444.
[58] H. Ali, L. Ma, H. Ghadbeigi, K. Mumtaz, *Mater. Sci. Eng. A* **2017**, *695*, 211.
[59] A. Shaji Karapuzha, D. Fraser, D. Schliephake, S. Dietrich, Y. Zhu, X. Wu, A. Huang, *J. Alloys Compd.* **2021**, *862*, 158034.
[60] T. Nitschke-Pagel, H. Wohlfahrt, in *Conference on Residual Stresses* (Eds: V. Hauk, H. Hougardy and E. Macherauch) Deutsche Gesellschaft für Materialkunde, Darmstadt, **1990**, pp. 121–133.
[61] A. Evans, G. Bruno, S. Cabeza, T. Mishurova, T. Pirling, I. Serrano-Munoz, M. Sprengel, A. Ulbricht, **2019**, https://doi.org/10.5291/ILL-DATA.1-02-276.